

Predictions of the Azimuthal Variation of the Noise from Chevron Jets using an Acoustic Analogy

S.J. Leib¹

HX5, LLC, NASA Glenn Research Center, Cleveland, Ohio 44135, USA

and

James E. Bridges²

National Aeronautics and Space Administration, John H. Glenn Research Center at Lewis Field, Cleveland, Ohio 44135, USA

An existing acoustic analogy formulation is used to make predictions of the turbulent mixing noise from a series of chevron jets tested at NASA Glenn Research Center. Reynolds-averaged Navier-Stokes solutions are used as input to provide the mean flow and turbulence quantities needed to compute the Green's function and parameterize the source model. The Green's function for the non-axisymmetric mean flows generated by these nozzles is computed using a second-order finite volume method. A slightly modified version of an existing source model originally developed for round jets is used to assess its capability in these non-axisymmetric flows. Prediction results are compared with experimental data for a range of azimuthal orders of the nozzle geometry and flow speeds. The results show that the RANS-based acoustic analogy prediction method is able to capture the observed azimuthal variation of the sound field fairly well at relatively low jet exit velocities. At higher speeds, the prediction method still captures the observed trends in azimuthal directivity but not the absolute levels, particularly at higher frequencies. Areas for potential improvement of the method are suggested.

I. Introduction

Non-circular nozzle exit geometries are often explored as a means to reduce or redirect noise from jet engine exhaust systems. Chevron nozzles are one widely studied class of non-circular geometries used for the reduction of peak noise levels and to tailor the sound directivity in desired ways. A review of the development of chevron technologies for jet noise reduction, from early fundamental studies of their impacts on flow and noise through their

¹ Senior Researcher, AIAA Senior Member.

² Acoustics Branch, AIAA Associate Fellow.

eventual implementation on modern jet engines, is given in Ref. [1]. Chevron nozzles present numerous geometrical parametric variations (chevron number, spacing, length, penetration) that can be varied in different combinations and it is desirable to understand and predict their effects on flow fields and radiated noise for optimal performance in given applications.

With rapid improvements in computer hardware and computational algorithms, large eddy simulations (LES) have been employed with increasing success in simulating details of high-speed unsteady turbulent flows and their noise radiation, including jet flows emanating from chevron nozzles. A small sampling of recent work can be found in Refs. [2]- [6]. In addition, Lattice Boltzmann simulations have also been used (Ref. [7]). Results from simulations such as these can provide a wealth of information on the flow and noise fields, with the former also being useful in informing lower-order prediction methods (Ref. [8]).

Such high-fidelity simulations do, however, still require very substantial computational resources and there is a need for low-order prediction methods which can be carried out more economically, even if they are limited to predicting differences in noise produced by geometric and flow-condition changes. Methods based on the Reynolds-averaged Navier-Stokes equations (RANS-based methods) provide a means to this end and are often used as an intermediate solution between large-scale numerical simulations and purely empirical methods, which are generally limited to the class of cases and physical features for which they were derived. RANS-based noise predictions in chevron jets were carried out in Refs. [9] - [11], for example.

A series of experiments was carried out at NASA Glenn Research Center, Ref. [12], in the Small Hot Jet Aeroacoustic Rig (SHJAR) (Ref. [13]) to systematically study the azimuthal directivity of noise produced by chevron nozzles with various levels of azimuthal mode order. These experiments built off of previous work on chevrons in this facility reported in Ref. [14]. In addition to providing insights into the azimuthal character of the noise from chevron jets, these experiments provide data that can be used to test and validate both high-fidelity and RANS-based noise predictions.

In this paper, an existing acoustic analogy formulation is used to make predictions of the turbulent mixing noise from the chevron nozzles tested at NASA Glenn (Ref. [12]). Reynolds-averaged Navier-Stokes (RANS) solutions are used as input to provide the mean flow and turbulence quantities needed to compute the Green's function and parameterize the source model. The Green's function for the non-axisymmetric mean flows generated by these nozzles

is computed using a second-order finite volume method in an attempt to capture the leading-order effects of the asymmetry. A slightly modified version of an existing source model, originally developed for round jets, is used to assess its capability in these non-axisymmetric flows. Prediction results are compared with experimental data for a range of azimuthal orders of the nozzle geometry and flow speeds. The results show that the RANS-based acoustic analogy prediction method is able to capture the observed azimuthal variation of the sound field fairly well at relatively low jet exit velocities. At higher speeds, the prediction method still captures the observed trends in azimuthal directivity but not the absolute levels, particularly at higher frequencies. Areas for potential improvement of the method are suggested.

II. The Acoustic Analogy

The jet noise prediction method used in this work is based on the Generalized Acoustic Analogy formulation of Refs. [15] and [16]. In this section we briefly review this formulation while presenting an extension of the original analysis to the case of a non-zero ambient flight stream. The extension to non-zero ambient flight stream is not used in this paper, but has been developed for use in future work. The form used for the predictions in this paper is obtained by setting the flight stream Mach number, $M_\infty = U_\infty/c_\infty$, where U_∞ is the free-stream velocity and c_∞ is the ambient speed of sound, equal to zero.

A. Formulation with flight stream

It is shown in Ref. [15] (see also Ref. [16]) that the acoustic spectrum at an observation point \mathbf{x} due to a unit volume of turbulence at source point \mathbf{y} can be written as

$$I_\omega(\mathbf{x}|\mathbf{y}) = (2\pi)^2 \Gamma_{\lambda j}(\mathbf{x}|\mathbf{y}; \omega) \int \Gamma_{kl}^*(\mathbf{x}|\mathbf{y} + \boldsymbol{\eta}; \omega) \mathcal{H}_{\lambda jkl}(\mathbf{y}, \boldsymbol{\eta}, \omega) d\boldsymbol{\eta}, \quad (1)$$

where the integration is over the source correlation volume, $\Gamma_{\lambda j}(\mathbf{x}|\mathbf{y}; \omega)$ is a ‘propagator’ function defined, for a locally parallel mean flow, by

$$\Gamma_{\lambda j}(\mathbf{x}|\mathbf{y}; \omega) = \int_{-\infty}^{\infty} \left[\frac{\partial}{\partial y_j} e^{ik(x_1 - y_1)} \hat{g}_{\lambda 4}^a(\mathbf{y}_T | \mathbf{x}_T; k, \omega) - (\gamma - 1) \delta_{\lambda 1} e^{ik(x_1 - y_1)} \frac{\partial U(\mathbf{y}_T)}{\partial y_j} \hat{g}_{44}^a(\mathbf{y}_T | \mathbf{x}_T; k, \omega) \right] dk, \quad (2)$$

where

$$\hat{g}_{\lambda 4}^a(\mathbf{y}_T | \mathbf{x}_T; k, \omega) = \frac{1}{(2\pi)^2} \iint e^{-i[k(x_1 - y_1) - \omega(t - \tau)]} g_{\lambda 4}^a(\mathbf{y}, \tau | \mathbf{x}, t) d(t - \tau) d(x_1 - y_1) \quad (3)$$

is the Fourier transform of the components of the adjoint vector Green's function, $g_{\lambda 4}^a(\mathbf{y}, \tau | \mathbf{x}, t)$, given by equations (4.8) – (4.11) of Ref. [15]. Star denotes the complex conjugate. Indices i, j range from one to three and λ, κ from one to four, with v'_i , $i = 1, 2, 3$ being the ordinary velocity fluctuation about the Favre-averaged velocity and $v'_4 = (\gamma - 1) \left(h' + \frac{1}{2} \right) v'^2$, where h' is the fluctuating enthalpy and γ the ratio of specific heats. The observer and source coordinates are represented by $\mathbf{x} = (x_1, \mathbf{x}_T)$ and $\mathbf{y} = (y_1, \mathbf{y}_T)$, respectively, with 1 being in the streamwise direction and T the transverse. The mean streamwise velocity, which depends only on the cross-flow coordinate \mathbf{y}_T , is denoted by $U(\mathbf{y}_T)$. The source spectrum $\mathcal{H}_{\lambda jkl}(\mathbf{y}, \boldsymbol{\eta}, \omega)$ is related to the spectrum,

$$H_{\lambda jkl}(\mathbf{y}, \boldsymbol{\eta}, \omega) = \frac{1}{2\pi} \int_{-\infty}^{\infty} e^{i\omega\tau} R_{\lambda jkl}(\mathbf{y}, \boldsymbol{\eta}, \tau) d\tau, \quad (4)$$

of the generalized Reynolds stress autocovariance tensor,

$$R_{\lambda jkl}(y, \boldsymbol{\eta}, \tau) = \lim_{T \rightarrow \infty} \frac{1}{2T} \int_{-T}^T [\rho v'_\lambda v'_j - \overline{\rho v'_\lambda v'_j}](\mathbf{x}, t) [\rho v'_\kappa v'_l - \overline{\rho v'_\kappa v'_l}](\mathbf{x} + \boldsymbol{\eta}, t + \tau) dt, \quad (5)$$

by

$$\mathcal{H}_{\lambda jkl} = \varepsilon_{\lambda j, \sigma m} H_{\sigma m \gamma n} \varepsilon_{\kappa l, \gamma n}, \quad (6)$$

where

$$\varepsilon_{\lambda j, \sigma m} \equiv \delta_{\lambda \sigma} \delta_{jm} - \frac{\gamma - 1}{2} \delta_{\lambda j} \delta_{\sigma m} \quad (7)$$

(see Refs. [15] and [16]).

For a locally parallel mean flow the components $\hat{g}_{\lambda 4}^a$ can be expressed in terms of a single (scalar), self-adjoint, Green's function as (equation (4.19) of Ref. [15])

$$\begin{aligned} \hat{g}_{14}^a(\mathbf{y}_T | \mathbf{x}_T; k, \omega) &= \frac{-ik\bar{c}^2(\mathbf{y}_T)}{(\omega - kU(\mathbf{y}_T))^2} \hat{G}_0(\mathbf{y}_T | \mathbf{x}_T; k, \omega) \\ \hat{g}_{i4}^a(\mathbf{y}_T | \mathbf{x}_T; k, \omega) &= \frac{\bar{c}^2(\mathbf{y}_T)}{(\omega - kU(\mathbf{y}_T))^2} \frac{\partial \hat{G}_0(\mathbf{y}_T | \mathbf{x}_T; k, \omega)}{\partial y_i}; i = 2, 3, \\ \hat{g}_{44}^a(\mathbf{y}_T | \mathbf{x}_T; k, \omega) &= \frac{-i}{(\omega - kU(\mathbf{y}_T))} \hat{G}_0(\mathbf{y}_T | \mathbf{x}_T; k, \omega) \end{aligned} \quad (8)$$

where $\bar{c}^2(\mathbf{y}_T)$ is the mean of the sound speed squared, which satisfies

$$\left\{ \frac{\partial}{\partial y_i} \frac{\bar{c}^2(\mathbf{y}_T)}{(\omega - kU(\mathbf{y}_T))^2} \frac{\partial}{\partial y_i} + 1 - \frac{k^2 \bar{c}^2(\mathbf{y}_T)}{(\omega - kU(\mathbf{y}_T))^2} \right\} \hat{G}_0(\mathbf{y}_T | \mathbf{x}_T; k, \omega) = \frac{\delta(\mathbf{x}_T - \mathbf{y}_T)}{(2\pi)^2}, i = 2, 3 \quad (9)$$

and

$$\hat{G}_0(\mathbf{y}_T | \mathbf{x}_T; k, \omega) = \hat{G}_0(\mathbf{x}_T | \mathbf{y}_T; k, \omega) \quad (10)$$

is a self-adjoint, scalar Green's function. Replacing \mathbf{y}_T with \mathbf{x}_T in (9), and using (10), it is shown that

$$\hat{G}_0(\mathbf{x}_T | \mathbf{y}_T; k, \omega) = \hat{G}_0(\mathbf{y}_T | \mathbf{x}_T; k, \omega) \sim \frac{e^{-x_T \sqrt{k^2 - (\omega - kU_\infty)^2 / c_\infty^2}}}{\sqrt{x_T}} \hat{\mathcal{G}}_0(\varphi, k, \omega | \mathbf{y}_T) \quad (11)$$

in the observer far-field, $x_T \rightarrow \infty$, where $U(\mathbf{x}_T) \rightarrow U_\infty$ and $\tilde{c}^2(\mathbf{y}_T) \rightarrow c_\infty^2$. Using (11) in (8) we can write

$$\hat{g}_{\lambda 4}^a(\mathbf{y}_T | \mathbf{x}_T; k, \omega) \sim \frac{e^{-x_T \sqrt{k^2 - (\omega - kU_\infty)^2 / c_\infty^2}}}{\sqrt{x_T}} \hat{\mathcal{G}}_{\lambda 4}(\varphi, k, \omega | \mathbf{y}_T). \quad (12)$$

Equation (12) can be inserted into (2) and the method of stationary phase applied to approximate the propagator function in the observer far field as

$$\Gamma_{\lambda j}(\mathbf{x} | \mathbf{y}; \omega) \rightarrow \frac{e^{i\omega \left(\frac{x}{1-M_\infty^2} \left[-M_\infty \cos \theta + \frac{\sqrt{1-M_\infty^2 \sin^2 \theta}}{1-M_\infty^2} \right] - y_1 \cos \theta^s \right) / c_\infty}}}{x} \sqrt{\frac{2\pi \omega \sin \theta}{c_\infty (1 - M_\infty^2 \sin^2 \theta)^{3/2}}} e^{-i\pi/4} \bar{\Gamma}_{\lambda j}(\mathbf{x} | \mathbf{y}_T; \omega), \quad (13)$$

where $M_\infty = U_\infty / c_\infty$, θ is the far-field observer polar angle relative to the downstream jet axis (ie. $\theta \equiv \sin^{-1}(x_T/x)$) and

$$\begin{aligned} \bar{\Gamma}_{ij}(\mathbf{x} | \mathbf{y}_T; \omega) = & e^{i\omega y_1 \cos \theta^s / c_\infty} \left\{ \frac{\partial}{\partial y_j} \frac{\tilde{c}^2 / \omega^2}{(1 - M \cos \theta^s)^2} \frac{\partial}{\partial y_i} e^{-i\omega y_1 \cos \theta^s / c_\infty} \hat{\mathcal{G}}_0(\varphi, k^{(s)}, \omega | \mathbf{y}_T) \right. \\ & \left. - \frac{i\delta_{i1}(\gamma - 1)}{\omega(M \cos \theta^s - 1)} \frac{\partial U}{\partial y_j} e^{-i\omega y_1 \cos \theta^s / c_\infty} \hat{\mathcal{G}}_0(\varphi, k^{(s)}, \omega | \mathbf{y}_T) \right\} \end{aligned} \quad (14)$$

and

$$\bar{\Gamma}_{4j}(\mathbf{x} | \mathbf{y}_T; \omega) = e^{i\omega y_1 \cos \theta^s / c_\infty} \frac{i}{\omega} \frac{\partial}{\partial y_j} e^{-i\omega y_1 \cos \theta^s / c_\infty} \frac{1}{(M \cos \theta^s - 1)} \hat{\mathcal{G}}_0(\varphi, k^{(s)}, \omega | \mathbf{y}_T), \quad (15)$$

where $M = U / c_\infty$ is the local acoustic Mach number and $k^{(s)} = \frac{\omega / c_\infty}{1 - M_\infty^2} \left\{ -M_\infty + \frac{\cos \theta}{\sqrt{1 - M_\infty^2 \sin^2 \theta}} \right\} \equiv \frac{\omega}{c_\infty} \cos \theta^s$ is the stationary phase point, which also defines θ^s .

In Refs. [15] and [16] arguments based on the relative disparity of the streamwise and transverse turbulence correlation and mean flow length scales were used to simplify (1); in particular to avoid integration of the propagator over the correlation volume while still accounting for retarded-time variations in the streamwise direction. Noting that

these effects are most significant when the Helmholtz number, $H = \omega D/c_\infty$, is order one or larger, the normalized far-field Green's function $\hat{g}_0^*(\varphi, k^{(s)}, \omega | \mathbf{y}_T)$ was represented by a Wentzel, Kramers, Brillouin and Jeffreys (WKBJ) - type form (Ref. [17])

$$\hat{g}_0^*(\varphi, k^{(s)}, \omega | \mathbf{y}_T) \approx A(\mathbf{x} | \mathbf{y}_T) e^{i \frac{\omega}{c_\infty} S(\varphi, \theta | \mathbf{y}_T)}, \quad (16)$$

where the amplitude function is expanded as

$$A(\mathbf{x} | \mathbf{y}_T) \approx A^{(0)}(\mathbf{x} | \mathbf{y}_T) + \frac{\omega}{c_\infty} A^{(1)}(\mathbf{x} | \mathbf{y}_T) + \left(\frac{\omega}{c_\infty}\right)^2 A^{(2)}(\mathbf{x} | \mathbf{y}_T) + \dots \quad (17)$$

Substituting (16), along with (11), in (9) for observers in the far-field, shows that $S(\varphi, \theta | \mathbf{y}_T)$ satisfies the Eikonal equation

$$(\nabla_{y_T} S) \cdot (\nabla_{y_T} S) = (1 - M(\mathbf{y}_T) \cos \theta^s)^2 \frac{c_\infty^2}{c^2(\mathbf{y}_T)} - \cos^2 \theta^s. \quad (18)$$

Equations (14) and (15) then imply that $\bar{\Gamma}_{kl}^*(\mathbf{x} | \mathbf{y}_T; \omega)$ can also be represented in WKBJ form so that

$$\bar{\Gamma}_{kl}^*(\mathbf{x} | \mathbf{y}_T; \omega) \approx A_{kl}(\mathbf{x} | \mathbf{y}_T) e^{i \frac{\omega}{c_\infty} S(\varphi, \theta | \mathbf{y}_T)}. \quad (19)$$

In Refs. [15] and [16] it is argued that $S(\varphi, \theta | \mathbf{y}_T)$ varies on the scale of the mean flow variation, which is long compared with the distance over which the turbulence is correlated, so that the propagator will be relatively constant over correlation volume and can be expanded in a Taylor series about \mathbf{y}_T

$$\bar{\Gamma}_{kl}^*(\mathbf{x} | \mathbf{y}_T + \boldsymbol{\eta}; \omega) \approx \bar{\Gamma}_{kl}^*(\mathbf{x} | \mathbf{y}_T; \omega) e^{i \frac{\omega}{c_\infty} \boldsymbol{\eta} \cdot \nabla_{y_T} S(\varphi, \theta | \mathbf{y}_T)}. \quad (20)$$

Using (13) and (20) in (1) shows that

$$I_\omega(\mathbf{x} | \mathbf{y}) = \frac{(2\pi)^2}{x^2} \frac{2\pi\omega \sin \theta}{c_\infty (1 - M_\infty^2 \sin^2 \theta)^{3/2}} \bar{\Gamma}_{\lambda j}(\mathbf{x} | \mathbf{y}_T; \omega) \bar{\Gamma}_{\kappa l}^*(\mathbf{x} | \mathbf{y}_T; \omega) \Phi_{\lambda j \kappa l}^* \left(\mathbf{y}, \frac{\omega \cos \theta^s}{c_\infty}, \frac{\omega}{c_\infty} \nabla_{y_T} S, \omega \right), \quad (21)$$

where

$$\Phi_{\lambda j \kappa l}^*(\mathbf{y}, k_1, \mathbf{k}_T, \omega) = \int e^{i k_1 \eta_1 + i \mathbf{k}_T \cdot \boldsymbol{\eta}_T} \mathcal{H}_{\lambda j \kappa l}(\mathbf{y}, \boldsymbol{\eta}, \omega) d\boldsymbol{\eta} = \int e^{i \mathbf{k} \cdot \boldsymbol{\eta}} \mathcal{H}_{\lambda j \kappa l}(\mathbf{y}, \boldsymbol{\eta}, \omega) d\boldsymbol{\eta}. \quad (22)$$

The formulation of Refs. [15] and [16] was developed for unheated jets, where the enthalpy source terms ($\lambda, \kappa = 4$) are set to zero. In this case the source spectrum, which reduces to $\Phi_{ijkl}^*(\mathbf{y}, k_1, \mathbf{k}_T, \omega); i, j, k, l = 1, 2, 3$, is symmetric in its first two and second two indices, and introducing the symmetric propagator function

$$G_{ij}(\mathbf{x}|\mathbf{y}_T) = G_{ji}(\mathbf{x}|\mathbf{y}_T) \equiv \frac{1}{2} [\bar{G}_{ij}(\mathbf{x}|\mathbf{y}_T) + \bar{G}_{ji}(\mathbf{x}|\mathbf{y}_T)], \quad (23)$$

it is shown that (21) can be written as

$$I_\omega(\mathbf{x}|\mathbf{y}) = \frac{(2\pi)^2}{x^2} \frac{2\pi\omega\sin\theta}{c_\infty(1 - M_\infty^2\sin^2\theta)^{3/2}} G_{ij}(\mathbf{x}|\mathbf{y}_T; \omega) G_{kl}^*(\mathbf{x}|\mathbf{y}_T; \omega) \Phi_{ijkl}^* \left(\mathbf{y}, \frac{\omega\cos\theta^s}{c_\infty}, \frac{\omega}{c_\infty} \nabla_{y_T} S, \omega \right) \quad (24)$$

for unheated jets.

The formulation of Refs. [15] and [16] also used an axisymmetric turbulence approximation to further reduce the number of independent source components that enter the formula for the acoustic spectrum. The final formula for the acoustic spectrum is expressed in terms of five independent components of the source spectral tensor

$$\Phi_{ijkl}^* \equiv \Phi_{ijkl}^* \left(\mathbf{y}, \frac{\omega\cos\theta^s}{c_\infty}, \frac{\omega}{c_\infty} |\nabla_{y_T} S|, \omega \right), \quad (25)$$

which is evaluated at the axial wavenumber corresponding to the stationary phase point, $k^{(s)} = \frac{\omega}{c_\infty} \cos\theta^s$, and, consistent with the axisymmetric turbulence approximation, depends only on the magnitude of the transverse wavenumber, $k_T = \frac{\omega}{c_\infty} |\nabla_{y_T} S| = \frac{\omega}{c_\infty} \sqrt{(1 - M(\mathbf{y}_T)\cos\theta^s)^2 \frac{c_\infty^2}{c^2(\mathbf{y}_T)} - \cos^2\theta^s}$, eliminating the need to solve the Eikonal equation. The formula for the acoustic spectrum (to the lowest-order approximation in the weakly non-parallel flow approximation), extended for the presence of a non-zero flight stream, is

$$\begin{aligned} I_\omega(\mathbf{x}|\mathbf{y}) = & \frac{(2\pi)^2}{x^2} \frac{2\pi\omega\sin\theta}{c_\infty(1 - M_\infty^2\sin^2\theta)^{3/2}} \left\{ [C^4 \Phi_{1111}^* + 2C(1 - C)\Phi_{1122}^* + (1 - C)^2 \Phi_{2222}^*] [\hat{g}_0]^2 \right. \\ & + 4 \left| \frac{\sqrt{\tilde{c}^2} \cos\theta^s}{c_\infty(1 - M\cos\theta^s)} \nabla_T \left(\frac{\sqrt{\tilde{c}^2} \hat{g}_0}{\omega(1 - M\cos\theta^s)} - \frac{(\gamma - 1)c_\infty}{2(1 - M\cos\theta^s)} (\nabla_T M) \hat{g}_0 \right) \right|^2 \Phi_{1212}^* \\ & \left. + 2(|G_{23}|^2 - Re \bar{G}_{22} \bar{G}_{33}^*) (\Phi_{2222}^* - \Phi_{2323}^*) \right\} \end{aligned} \quad (26)$$

where $\hat{g}_0 = \hat{g}_0(\varphi, k^{(s)}, \omega | \mathbf{y}_T)$, the propagator functions G_{ij} and \bar{G}_{ij} are evaluated at the stationary phase point $k^{(s)} = \frac{\omega}{c_\infty} \cos\theta^s$ and

$$C^2 = \frac{\tilde{c}^2 \cos^2\theta^s}{c_\infty^2(1 - M\cos\theta^s)^2}. \quad (27)$$

When combined with a model for the source terms and integrated over the source volume, equation (26) provides a formula for the prediction of the mixing noise from an unheated turbulent jet.

B. Green's function

For the noise predictions in this paper, the mean flow is represented by a unidirectional transversely sheared mean flow for which the adjoint vector Green's function can be expressed in terms of a single scalar function. For observer locations in the far field, the relevant problem for the Green's function can be reduced to (see Ref. [18])

$$\left\{ \frac{\partial}{\partial y_i} \frac{\tilde{c}^2(\mathbf{y}_T)}{(1 - M(\mathbf{y}_T) \cos \theta^s)^2} \frac{\partial}{\partial y_i} + \omega^2 \left(1 - \frac{\tilde{c}^2(\mathbf{y}_T) / c_\infty^2}{(1 - M(\mathbf{y}_T) \cos \theta^s)^2} \right) \right\} \tilde{g}(\mathbf{y}_T; \varphi, \theta, \omega) = 0 ; i = 2, 3 , \quad (28)$$

where $\tilde{g}(\mathbf{y}_T; \varphi, \theta, \omega) \equiv \tilde{g}_0(\varphi, k^{(s)}, \omega | \mathbf{y}_T)$ is the Green's function appearing in the formula for the acoustic spectrum (26), subject to the far-field (in the source coordinate) boundary condition

$$\frac{\partial \tilde{g}(\mathbf{y}_T; \varphi, \theta, \omega)}{\partial y_T} + \kappa \tilde{g}(\mathbf{y}_T; \varphi, \theta, \omega) \rightarrow T, \quad (29)$$

with

$$T = \frac{-i\omega \sin \theta [1 + \cos(\varphi - \varphi_0)] (\omega / c_\infty)^2 e^{\frac{-i\omega}{c_\infty} y_T \sin \theta \cos(\varphi - \varphi_0) / \sqrt{1 - M_\infty^2 \sin^2 \theta}} e^{i\pi/4}}{c_\infty \sqrt{1 - M_\infty^2 \sin^2 \theta} \quad 2(2\pi)^2 \sqrt{2\pi \omega \sin \theta / c_\infty}} [1 - M_\infty \cos \theta^s]^2 (1 - M_\infty^2) \quad (30)$$

and

$$\kappa = \frac{-i\omega \sin \theta}{c_\infty \sqrt{1 - M_\infty^2 \sin^2 \theta}} \quad (31)$$

as $y_T \rightarrow \infty$, $\varphi = \tan^{-1}(x_3 / x_2)$ is the observer azimuthal angle and $\varphi_0 = \tan^{-1}(y_3 / y_2)$ the source azimuthal angle.

Given the mean acoustic Mach number and sound speed profiles, (28)–(31) can be solved numerically and the method used in this work is described in Subsection D below.

C. Source model

For the noise predictions presented in this paper, the source model is the hybrid (space-time/spectral) model of Ref. [16]. The model provides a formula for the source spectral function,

$$\Psi_{ijkl}^*(\mathbf{y}; \mathbf{k}, \omega) = \int_V e^{i\mathbf{k}\cdot\boldsymbol{\eta}} H_{ijkl}(\mathbf{y}, \boldsymbol{\eta}, \omega) d\boldsymbol{\eta}, \quad (32)$$

which is related to the source function $\Phi_{ijkl}^*(\mathbf{y}; \mathbf{k}, \omega)$ in (26), by $\Phi_{ijkl}^* = \varepsilon_{ij,pm} \Psi_{pmqn}^* \varepsilon_{kl,qn}$, as

$$\Psi_{ijkl}^*(\mathbf{y}; \mathbf{k}, \omega) = -\frac{\pi l_0 l_1 \bar{l}_T^2 (1 + \tilde{\omega}^2)^{1/2} A_{ijkl}}{U_c} \sum_{m,l=0}^{\infty} a_{m,l} (-1)^{m+l} D_{k_1}^m D_{\omega}^l \frac{1}{R} \frac{\partial}{\partial R} \frac{1}{(1+R^2)} e^{-\tilde{k}_T^2 / 4(1+R^2)^{1/2}}, \quad (33)$$

where A_{ijkl} are amplitude factors, $a_{m,l}$ are constants, $l_i, i = 0,1,2,3$ are turbulent length scales evaluated from the RANS solution as $l_i = C_i k^{3/2} / \epsilon$, where k is the turbulent kinetic energy, ϵ the dissipation rate and the C_i are constants. The frequency-dependent transverse length scale, \bar{l}_T , is modeled as

$$\bar{l}_T = \frac{l_{2,3} \sqrt{2}}{[1 + \tilde{\omega}^2 (1 + b\tilde{\omega}^3)/(1 + b)]^{1/4}} \quad (34)$$

where b is a constant. The normalized frequency is defined as $\tilde{\omega} \equiv \omega l_0 / U_c$, with ω the radian frequency and U_c the convection velocity of the turbulence. $\tilde{k}_T^2 \equiv (k_2^2 + k_3^2) \bar{l}_T^2 (1 + \tilde{\omega}^2)^{1/2}$ is a normalized transverse wavenumber, $R^2 \equiv \tilde{\omega}^2 + \tilde{k}_1^2$ and $\tilde{k}_1 \equiv (k_1 - \omega / U_c) l_1$. The operators D_{k_1} and D_{ω} , are defined as

$$D_{k_1} \equiv \left(\frac{l_1}{l_0} \frac{\partial}{\partial \tilde{\omega}} + \frac{\partial}{\partial \tilde{k}_1} \right) \left(\frac{l_1}{l_0} \tilde{\omega} + \tilde{k}_1 \right); \quad D_{\omega} \equiv \frac{\partial}{\partial \tilde{\omega}} \tilde{\omega}. \quad (35)$$

As in Ref. [16] four terms, corresponding to the coefficients $a_{0,0}, a_{0,1}, a_{0,2}, a_{0,3}$, in the summation in (33) are used in this work.

D. Numerical Methods

For the non-axisymmetric mean flows considered in this paper, the Green's function in equations (28) – (31) is solved numerically using a simple, second-order finite volume method. The general approach is described in Ref. [19]. A polar cylindrical grid is constructed at selected axial slices in the flow. A full three-hundred-sixty degree azimuthal domain is considered with radial extent of six nozzle diameters. Axial locations ranging from two to twenty diameters from the nozzle exit are included in the calculations. Equation (28) is integrated over each area element for this two-dimensional problem, and use of the divergence theorem results in a sum of line and area integrals. In this way derivatives of the mean flow (streamwise velocity and mean sound speed) in the first term of (28) are eliminated. Line integrals are approximated by the mid-point rule and second-order central differences are used for derivatives of the

Green's function, $\partial g / \partial y_T$ and $\partial g / \partial \varphi_0$ in the radial and azimuthal directions, respectively. Area integrals are also approximated by the mid-point rule and second-order averages are used to obtain the cell area. The solution value on the center of the domain is obtained as the average of those surrounding it at the first off-axis radial location (see Ref. [20]). Symmetry conditions are used to close the system in the azimuthal direction. The far-field boundary condition (29) – (31) is implemented using a second-order backward difference to approximate the radial derivative. The resulting linear system of equations is solved using a standard banded solver. Further details can be found in Ref. [21].

Once the Green's function is computed, it is inserted into (26) and the result integrated over the source volume using the trapezoidal rule to obtain the acoustic spectrum.

III. Test Cases

Test cases are taken from experiments conducted at NASA Glenn Research Center described in Ref. [12]. Figure 1 shows the geometries of the nozzles, and Table 1 the matrix of flow conditions, selected for use in this paper. The nozzles, which have a nominal exit diameter (D), of two inches, are presented in order of decreasing mode order (increasing asymmetry). The three nozzles chosen have azimuthal mode orders of three, four and five; mode orders higher than six produce noise with a very small deviation from axisymmetry. Jet exit acoustic Mach numbers range from 0.5 to 0.9; all cases are unheated, resulting in slightly cold jets exiting the nozzle.



Figure 1. Nozzles selected from Ref. [12] and predictions.

Table 1 - Flow conditions

Set Point (SP)	$Ma = U_J/c_\infty$	T_{static}/T_∞
3	0.5	0.95
5	0.7	0.90
7	0.9	0.84

IV. Results

Reynolds-averaged Navier-Stokes (RANS) solutions for the mean streamwise velocity and temperature are used to compute the Green's function in equations (28) – (31), and the turbulent kinetic energy and dissipation rate are combined to determine the length scales in the source model in Section II C. All RANS flow solutions were computed using the MentorGraphics® Flow Simulation package available through Dassault Systeme's SolidWorks®. Unstructured solutions were exported and interpolated onto a structured grid suitable for use in the noise calculations. In the next sub-section selected results from these RANS solutions are compared with available mean flow data and the azimuthal character of the mean flow and turbulence distributions are discussed.

A. RANS Solutions

1. Comparisons with experimental data

Mean flow data available from total pressure surveys in the SMC004 and SCM002 nozzles at SP7 (Ref. [14]) is used to partially validate the RANS solutions used as input to the noise prediction method.

Figure 2 shows mean acoustic Mach number contours (mean axial velocity normalized by the ambient sound speed) in cross-flow planes at several axial locations downstream of the nozzle exit computed from RANS and obtained from experimental data in the SMC004 nozzle at SP7. The comparisons are shown as pairs of contour plots at axial locations downstream of the nozzle exit of $y_1/D = 0.5, 1.0, 2.0, 5.0, 10.0$, with the RANS solution on the left and experimental data on the right. The contours from the interpolated RANS solutions are very similar to those for the mean velocity estimated from the total pressure surveys. In particular, the azimuthal character of the mean flow, as well as its eventual relaxation to axi-symmetry seems to be well represented by the RANS.

Figure 3 shows comparisons of the mean streamwise velocity, normalized by the jet exit velocity, U_J , on the jet centerline as a function of normalized axial distance from the nozzle exit extracted from the RANS and the data. The experimental data is somewhat sparse, but the RANS appears to capture the extent of the potential core and initial downstream decay reasonably well, but seems to mix out a bit too rapidly further downstream.

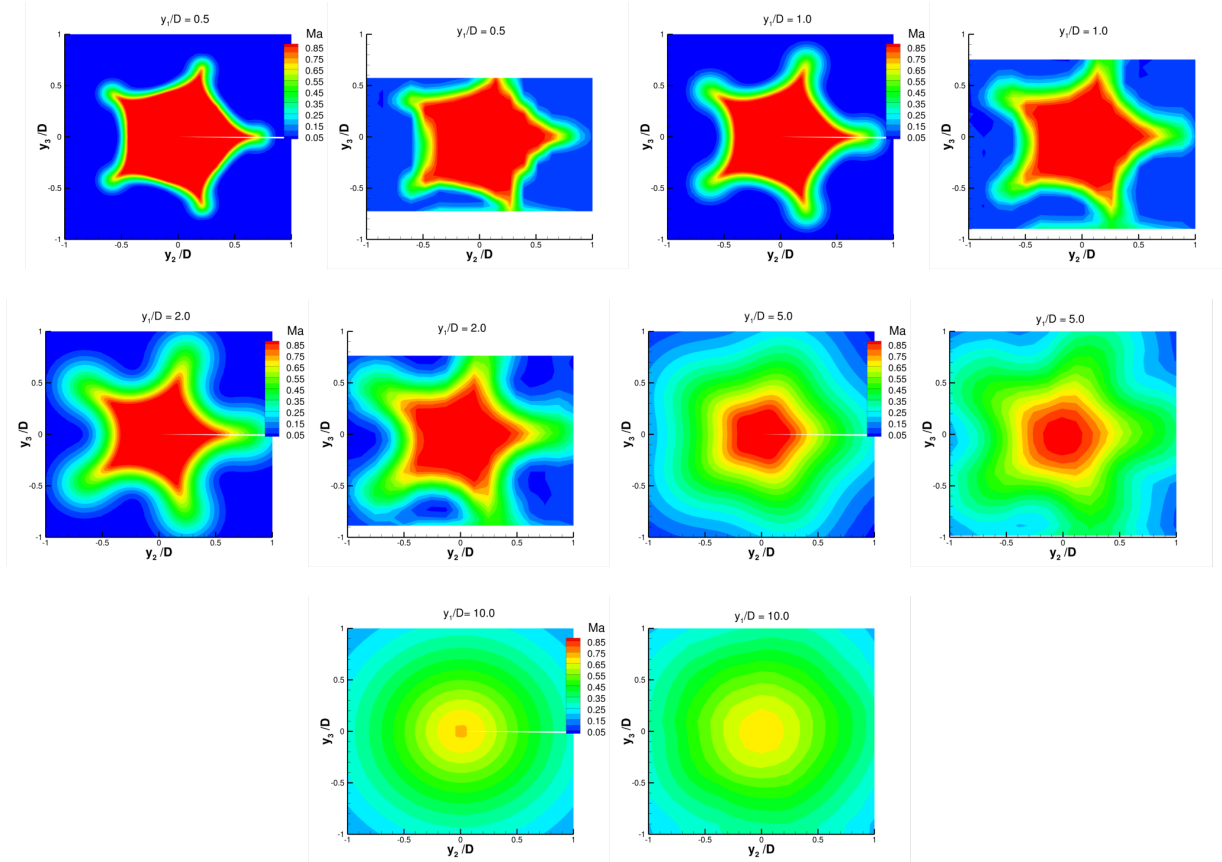


Figure 2 -- Comparisons of acoustic Mach number contours at different axial locations downstream of the nozzle exit for SMC004 SP7. Left – RANS ; Right – Experiment (Ref. [14]).

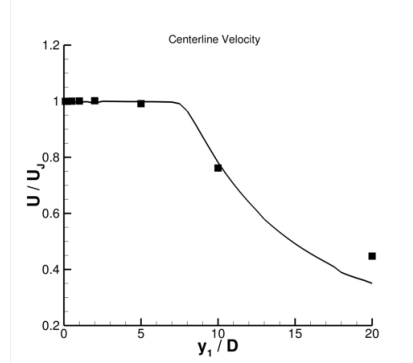


Figure 3 - Normalized mean streamwise velocity on the jet centerline vs. normalized axial location from the nozzle exit. SMC004 SP7. RANS – Solid line ; Experiment (Ref. [14]) – Symbols.

Figure 4 and 5 show corresponding comparisons for the SMC002 nozzle. The asymmetry of the mean flow in this jet is also well captured by the RANS solution in this case, with the jet exhibiting ‘thick’ and ‘thin’ sides for some distance downstream before becoming axisymmetric by about ten diameters from the exit. The normalized mean streamwise velocity on the jet centerline (Figure 5) also exhibits similar agreement to that for the SMC004 nozzle.

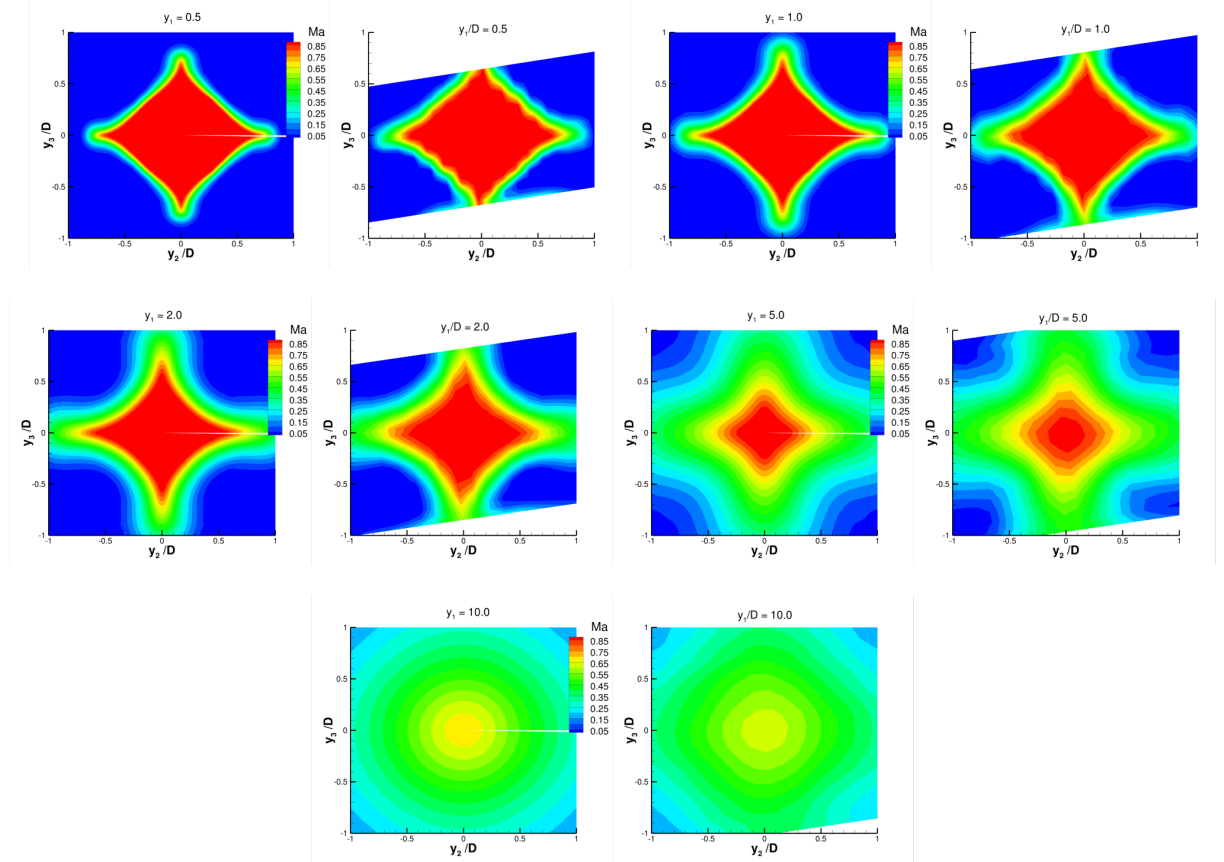


Figure 4 – Comparisons of acoustic Mach number contours at different axial locations downstream of the nozzle exit for SMC002 SP7. Left – RANS ; Right – Experiment ([14]).

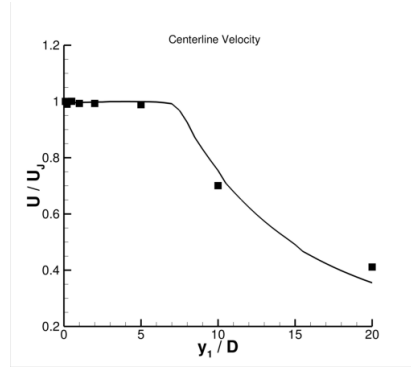


Figure 5 – Normalized mean streamwise velocity on the jet centerline vs. normalized axial location from the nozzle exit. SMC002 SP7. RANS – Solid line ; Experiment ([14]) – Symbols.

These comparisons do not constitute a complete validation of the mean flow and turbulence computed from the RANS, but they provide some confidence that the primary asymmetric feature of the flows are reasonably well captured and that the RANS solutions can be used as input to predict azimuthal variations in the sound field.

2. Mean velocity and turbulent kinetic energy

Figure 6 shows interpolated RANS results for contours of mean acoustic Mach number and normalized turbulent kinetic energy for the SMC004 nozzle at SP3, and Figure 7 the corresponding results at SP7, at an axial location five diameters from the nozzle exit. The jet exit velocity corresponding to the nozzle pressure ratio and nominal nozzle exit diameter are used in the normalization. The SMC004 nozzle produces the least asymmetry of those chosen here from the cases tested in the work of Ref. [12]. There are slight indications of ‘thick’ (white line) and ‘thin’ (red line) sides to the jet, as characterized by the mean flow, corresponding to regions of relatively low and high, respectively, turbulence levels. The azimuthal variations are somewhat more pronounced at the higher speed (Figure 7).

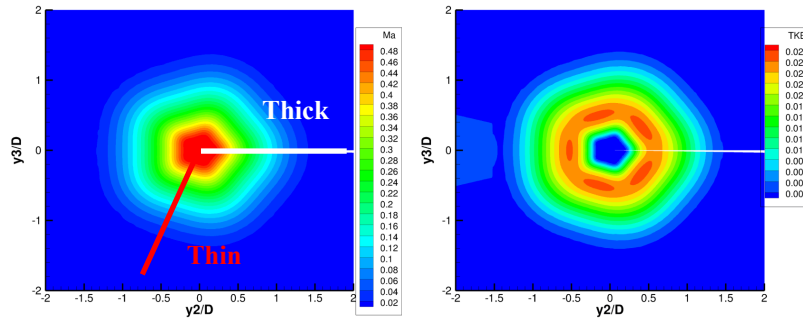


Figure 6. Contours of: (Left) acoustic Mach number ; (Right) normalized turbulent kinetic energy. SMC004, SP3.

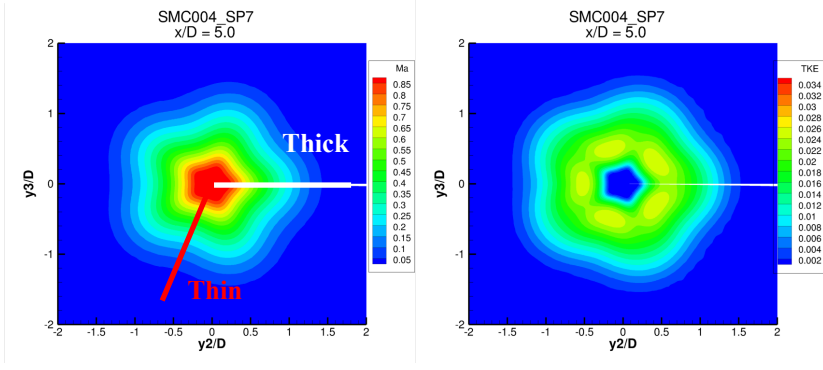


Figure 7. Contours of: Left, acoustic Mach number ; Right, normalized turbulent kinetic energy. SMC004, SP7.

Figure 8 and 9 show corresponding RANS solutions for the SMC002 nozzle. This case shows more pronounced asymmetry in terms of the mean flow and turbulence levels. Comparing these figures shows that the asymmetry is again more pronounced at the higher jet speed.

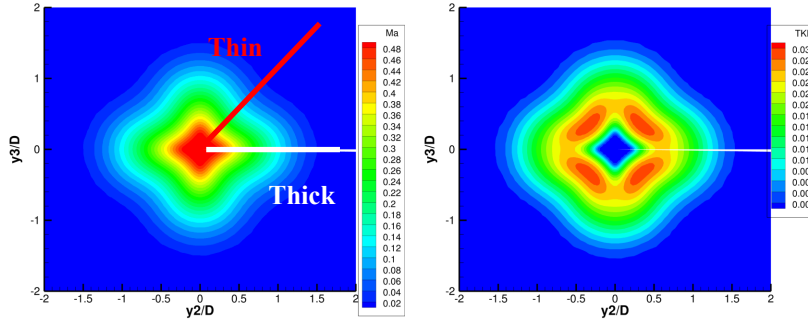


Figure 8. Contours of: Left, acoustic Mach number ; Right, normalized turbulent kinetic energy. SMC002, SP3.

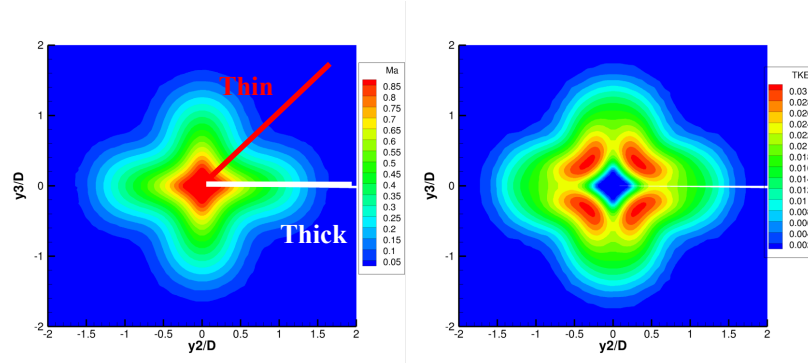


Figure 9. Contours of: Left, acoustic Mach number ; Right, normalized turbulent kinetic energy. SMC002, SP7.

Figure 10 shows RANS results for the SMC026 nozzle at SP3, and Figure 11 the corresponding results at SP7, also at five diameters downstream of the nozzle exit. This nozzle produces the most asymmetry of the chevron jets tested in Ref. [12], with these being quite strong at SP7. A relative increase in turbulence level of nearly ten percent is seen between the ‘thin’ and ‘thick’ sides of this jet at this axial location.

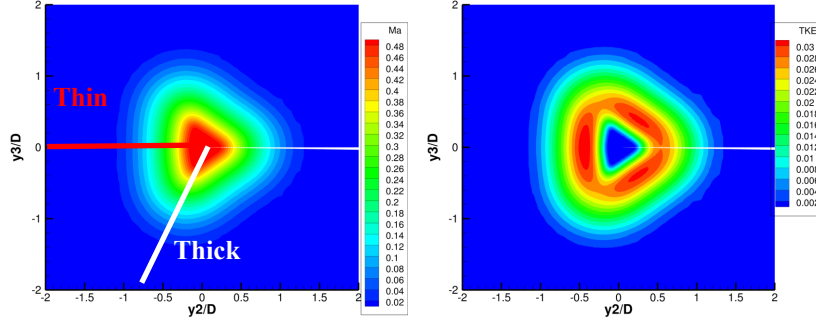


Figure 10. Contours of: Left, acoustic Mach number ; Right, normalized turbulent kinetic energy. SMC026, SP3.

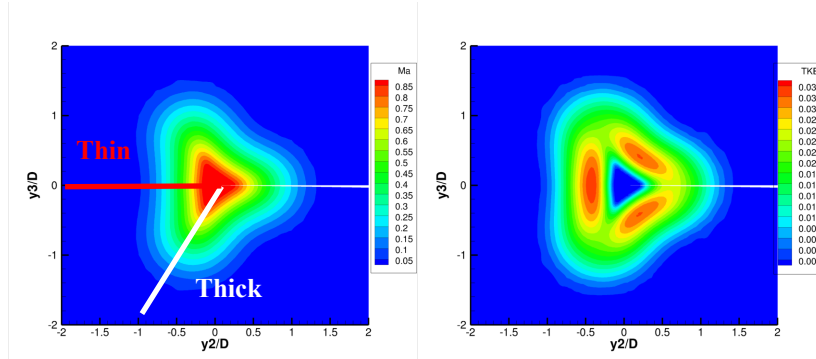


Figure 11 Contours of: Left, acoustic Mach number ; Right, normalized turbulent kinetic energy. SMC026, SP7.

The observations from the flow solutions above can provide some expectations as to the ultimate azimuthal variation of the sound fields for the various cases and help to anchor reference locations for the discussion of the noise prediction results. These are presented in the next section.

B. Noise Predictions

The noise prediction results presented in this paper use the hybrid model of Ref. [16] with slightly modified coefficients for the Ψ_{1212} and Ψ_{2222} source spectral components. This model was originally developed and tuned for

high-speed round unheated jets with RANS solutions obtained from an early version of the Wind-US code. Part of the objective of this work is to assess the suitability of this model for use in chevron jets and expose areas in need of improvement. For completeness, the values of these coefficients are given here.

Source component amplitudes are set as, $R_{ijkl}(\mathbf{y}, \mathbf{0}, 0) = C_{ijkl}(\bar{\rho}k)^2$ where C_{ijkl} are constants adopted from Ref. [16]: $C_{1111} = 1.28$, $C_{2222} = C_{3333} = 0.3$, $C_{1122} = C_{1133} = 0.0616$, $C_{1212} = 0.2918$. The constant b in the transverse frequency-dependent length scale (34) is set to 0.5 for the 1212 component and 0.1 for all others. The turbulent convection velocity is set to $U_c = 0.8U_{CL}$ for the 1212 component and $U_c = 0.68U_{CL}$ for all others, where U_{CL} is the jet centerline velocity. The source coefficients for the truncated series representation of the source spectral components and length scales are given in Table 2 and Table 3.

Table 2 - Coefficients in truncated series for turbulence spectrum (33).

Component	$a_{1,0}/a_{0,0}$	$a_{2,0}/a_{0,0}$	$a_{3,0}/a_{0,0}$
1111	0.073	0.070	-0.0008
2222=3333	0.519	0.049	-0.0097
1122 = 1133	0.103	0.079	0.0
1212	0.388	-0.126	-0.031

Table 3 - Constants used in length scales.

Component	C_0	C_1	C_T
1111	0.7	1.2	0.4
2222=3333	0.7	0.8	0.89
1122 = 1133	0.7	1.05	1.0
1212	1.05	1.0	1.1

Figures 12 – 20 show comparisons of the acoustic spectrum (power spectral density of the far-field fluctuating pressure per unit Strouhal number, $St = fD/U_J$, where f is frequency, D the nozzle diameter and U_J the jet exit velocity, referenced to 2×10^{-5} Pa) computed from the noise prediction method with experimental data for these chevron nozzles at observer polar angles of ninety, sixty and thirty degrees from the downstream jet axis and observer azimuthal angles corresponding to the ‘thick’ and ‘thin’ sides (as indicated on Figures 6-11) of the jets for SPs 3, 5 and 7.

Absolute noise prediction levels are generally within a few dB of the data and the spectral shapes compare reasonably well for most cases and angles. The largest discrepancies are at the intermediate polar angle, $\theta = 60^\circ$, which has been noted even in some previous comparisons for axisymmetric jets. Our primary interest here is in the relative azimuthal variation of the noise, especially the differences in noise radiated to the ‘thick’ and ‘thin’ sides from the different nozzles at different conditions. The SMC004 nozzle (Figures 12 - 14) shows very little difference in noise radiated to the ‘thick’ and ‘thin’ sides; the very small variations seen in the data at the higher frequencies and speeds are not picked up by the predictions. The SMC002 nozzle (Figures 15 - 17) shows a bit more azimuthal variation in

the noise radiated to the ‘thick’ and ‘thin’ sides at the highest jet speed and downstream angles, with the predictions capturing the general trends. The SMC026 nozzle (Figures 18 – 20) show the largest azimuthal variation, with difference between the ‘thick’ and ‘thin’ sides of several dB at the higher speeds and downstream angles.

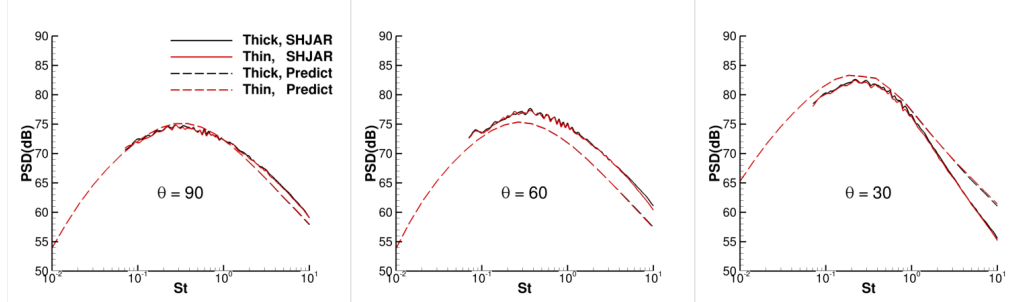


Figure 12 - Comparisons of noise predictions with data. SMC004 SP3

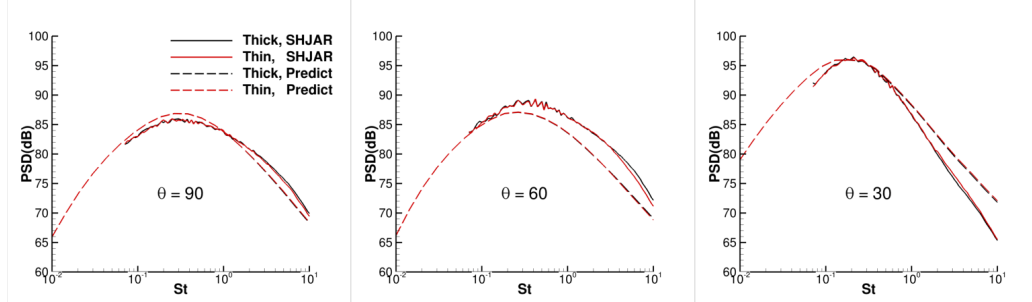


Figure 13 - Comparisons of noise predictions with data. SMC004 SP5

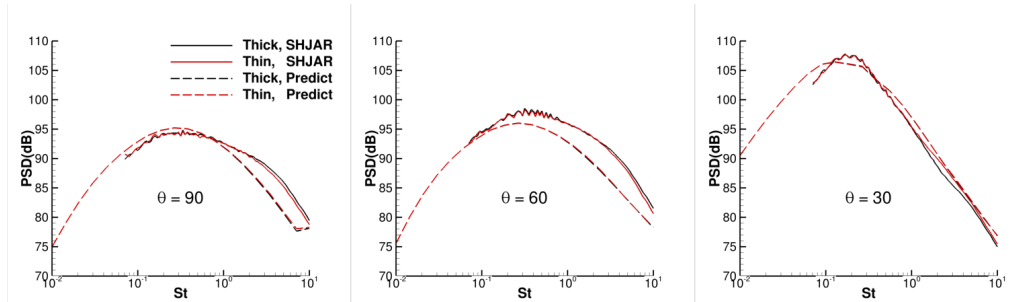


Figure 14 - Comparisons of noise predictions with data. SMC004 SP7

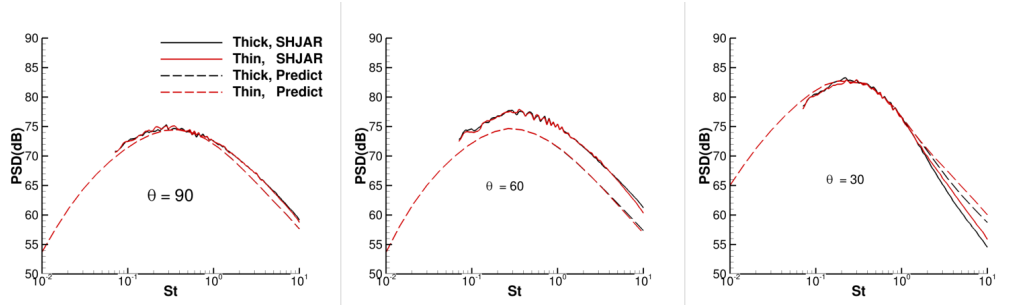


Figure 15. Comparisons of noise predictions with data. SMC002, SP3.

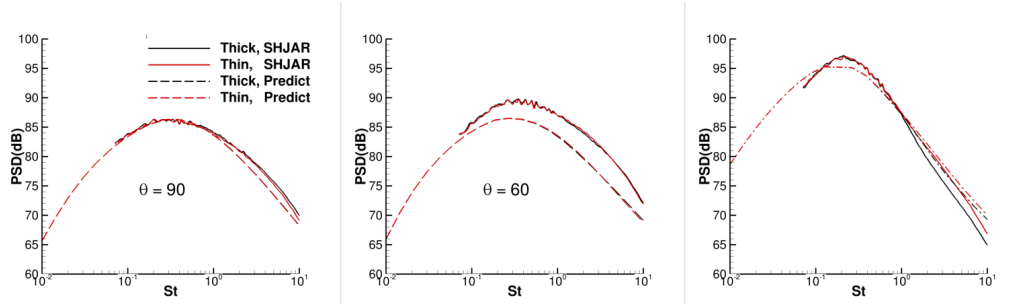


Figure 16. Comparisons of noise predictions with data. SMC002, SP5.

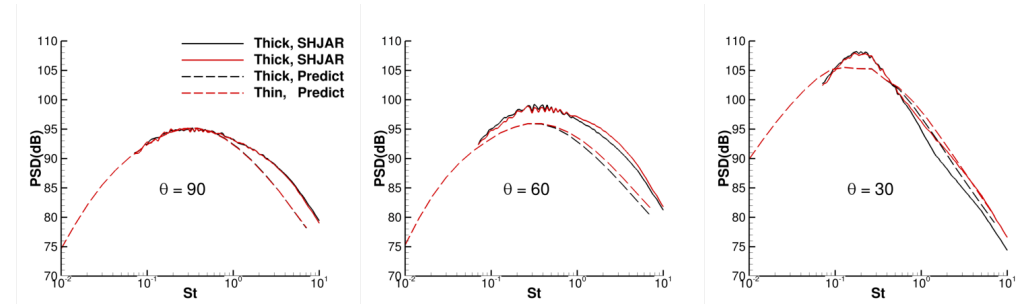


Figure 17. Comparisons of noise predictions with data. SMC002, SP7.

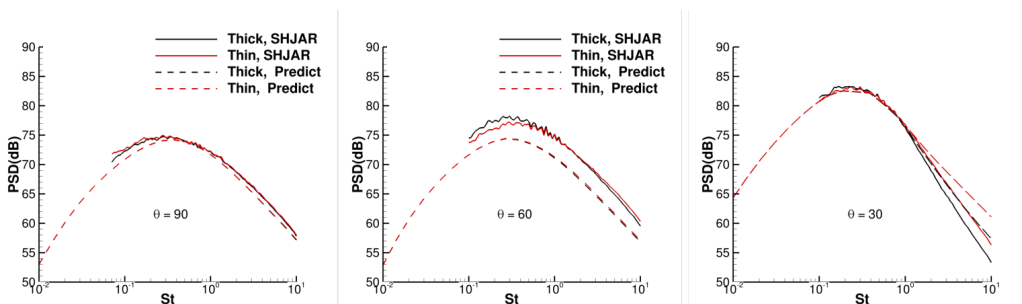


Figure 18 - Comparisons of noise predictions with data. SMC026 SP3.

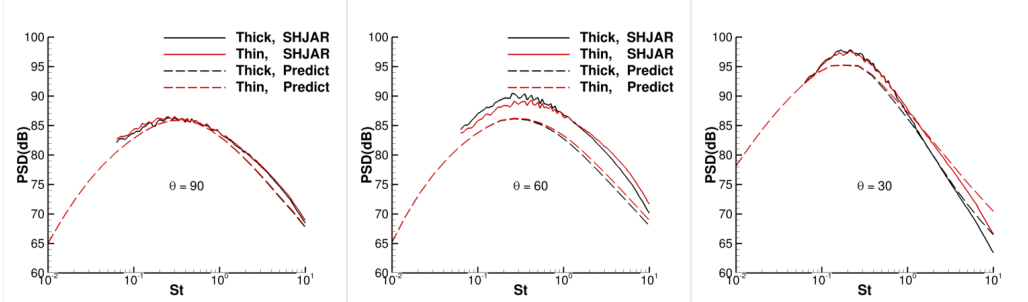


Figure 19 - Comparisons of noise predictions with data. SMC026 SP5.

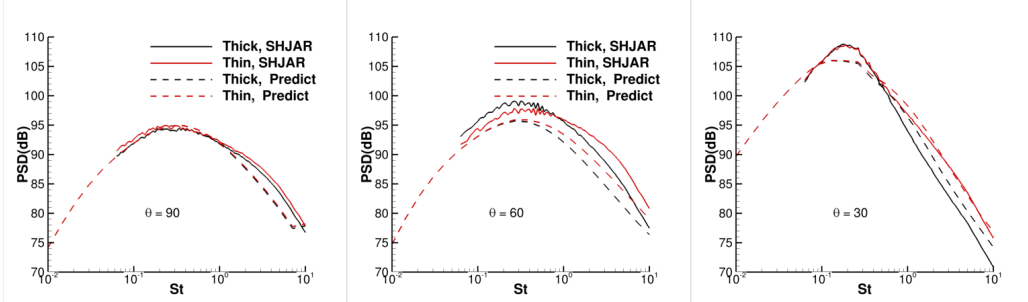


Figure 20 - Comparisons of noise predictions with data. SMC026 SP7.

A more quantitative look at the ability of the prediction method to capture the leading-order differences in noise radiated to the ‘thick’ and ‘thin’ sides of the chevron jets is given in Figure 21 and Figure 22. The differences (in terms of dB levels) between the noise radiated to the ‘thin’ and ‘thick’ sides are plotted vs. Strouhal number at three polar angles, at the three flow conditions considered, for the SMC002 and SMC026 nozzles, respectively. The comparisons show that the predictions do a good job of quantitatively capturing these differences at the lowest jet speed (SP3 in Figure 21(a) and Figure 22 (a)) for both nozzles over nearly the entire frequency range. The quantitative agreement is still fairly good for the SMC026 nozzle (the most asymmetric one) at the intermediate speed (Figure 22(b)), but less so for the SMC002 one (Figure 21 (b)). At the highest speed considered here (Figures 21 (c) and 22(c)) the predictions begin to capture the onset of azimuthal asymmetry at around $St = 1.0$, but do not capture the larger differences seen in the data at higher frequencies. For nearly all cases considered the quantitative agreement breaks down at the highest frequencies, but the general trends in the data are still followed, including the increase in noise radiated to the ‘thin’ side at the intermediate angle ($\theta = 60^\circ$) at SP5 in the SMC026 nozzle and SP7 in both. We

note that the model fails to capture the experimentally observed relative increase in noise radiated to the ‘thick’ of the jet at lower frequencies at the intermediate angle in the SMC026 nozzle.

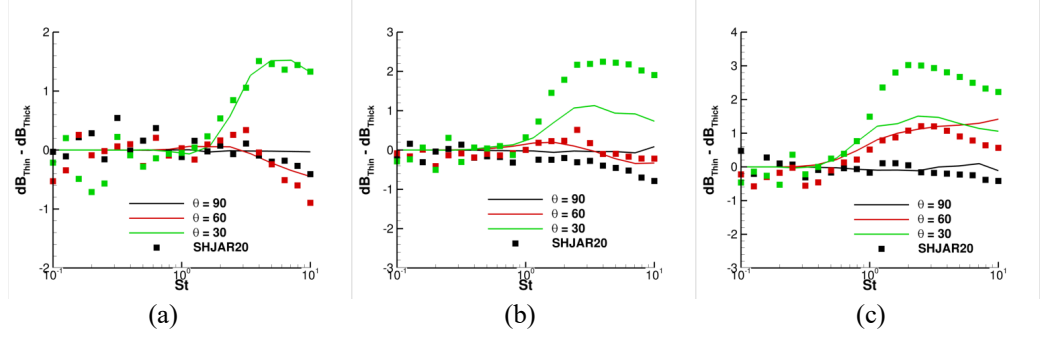


Figure 21. Difference in the sound field radiated to the ‘thin’ and ‘thick’ sides vs. Strouhal number: SMC002

(a), SP3. (b), SP5, (c), SP7.

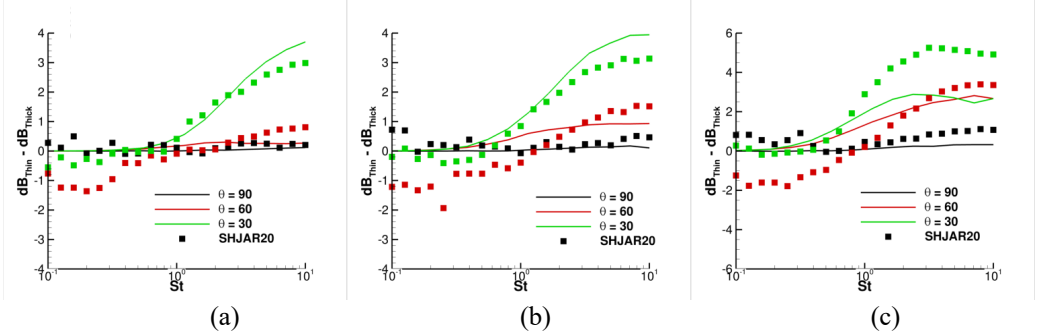


Figure 22. Difference in the sound field radiated to the ‘thin’ and ‘thick’ sides vs. Strouhal number: SMC026.

(a), SP3, (b), SP5, (c), SP7.

A bit more detail on the azimuthal character of the noise radiated by the SMC002 and SMC026 nozzles is shown in Figure 23 and 24, where plots of the azimuthal directivity, relative to the ‘thick’ side of the jet, of the difference between the sound radiated in a given azimuth and that in the ‘thick’ direction are shown. The red dashed lines correspond to azimuthal angles where the jet is ‘thin’. Like the results from the ‘thick’ and ‘thin’ sides (Figure 21 and Figure 22), these plots show that, for the lower speed case, as long as the frequency is not too large (St less than around 9.0) the relative azimuthal variation of the predictions from these two jet compare reasonably well with data. As the jet speed increases, the agreement deteriorates, particularly for the SMC002 nozzle where there is less azimuthal

directivity. At the highest speed (SP7), even in the most asymmetric nozzle (SMC026), the predictions do not reach the relatively large absolute levels of azimuthal variation seen in the data, although the general trends are still captured.

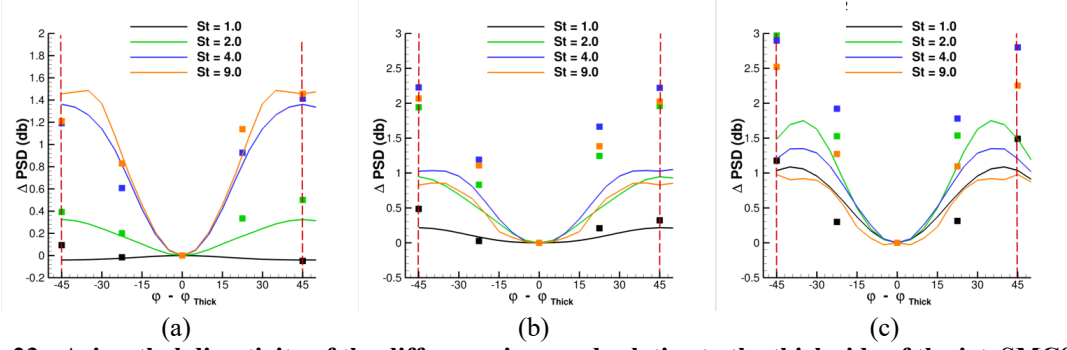


Figure 23 - Azimuthal directivity of the difference in sound relative to the thick side of the jet. SMC002. (a) SP3 ; (b) SP5 ; (c) SP7.

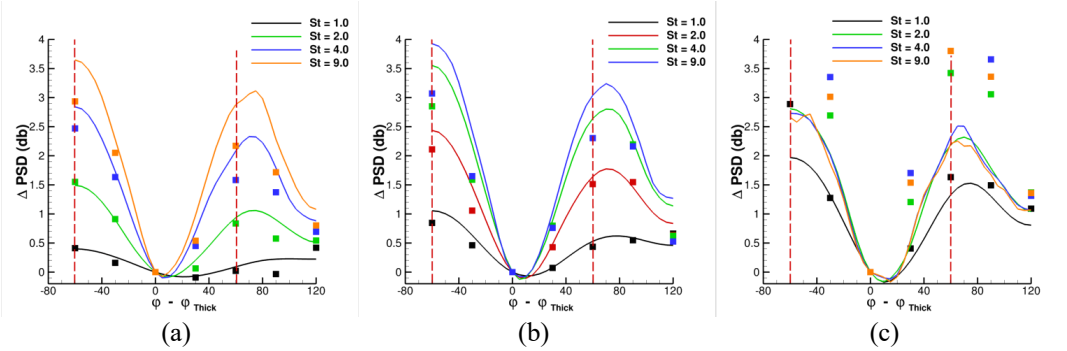


Figure 24 - Azimuthal directivity of the difference in sound relative to the thick side of the jet. SMC026. (a) SP3 ; (b) SP5 ; (c) SP7.

V. Summary and Conclusions

In this paper an existing acoustic analogy formulation and source model are used to make predictions of the turbulent mixing noise for a series of chevron jets. The predictions are compared with experimental data taken at NASA Glenn Research Center during a test of chevron nozzles to systematically study their azimuthal sound fields as the nozzle modal-order and flow conditions are changed. Input to the noise prediction method is supplied by RANS solutions. These solutions are partially validated here by comparing with mean streamwise velocities obtained from total pressure surveys from an earlier test at NASA Glenn.

The noise prediction results presented in this paper show that the model is able to capture the azimuthal directivity of the sound field in the jets at lower Mach numbers and frequencies, but gives poorer results at the higher speeds and higher frequencies. Although the general trends appear to be consistent with observations, the predicted deviation from axisymmetry is not as great as was found in the experiments.

The relatively low order of the numerical method used to solve for the Green's function is a likely cause for the breakdown of the predictions at higher frequencies and higher speeds. Refinements in the grid on which the Green's function is solved, particularly in the azimuthal direction, have been found to improve results, but memory and computing-time constraints become prevent this from being a useful fix, particularly for a reduced-order model which is meant to provide relatively quick results.

The source model used in this work was originally developed for a round jet. Part of the goal of this work was to determine if, and over what parameter range, this model could be used in more complex jets, like those emanating from chevron nozzles. Although the implementation of this source model for the chevron nozzles considered here makes use of local values of the turbulent kinetic energy and dissipation rate as computed by RANS, it may not fully capture the azimuthal character of the source, particularly the azimuthal dependence of the eddy convection velocity, which is known to be an important quantity in jet noise predictions, especially at high speeds (see Ref. [22]).

The failure of the model to capture the relative increase in noise radiated to the ‘thick’ of the jet at low frequencies at the intermediate angle in the SMC026 nozzle could perhaps be due to neglecting the jet spreading in the axial direction (parallel mean flow approximation), which may be more pronounced in this highly non-axisymmetric flow. It is known that non-parallel mean flow effects enter the problem for the Green’s function at the leading-order at low frequencies (see Ref. [23]).

Acknowledgment

This work was supported by the Commercial Supersonic Technology Project under the NASA Advanced Air Vehicle Program. The authors thank Mr. Brian Heberling of NASA Glenn for his comments on the paper.

References

- [¹] Zaman, K.B.M.Q, Bridges, J.E. and Huff, D.L., “Evolution from ‘Tabs’ to ‘Chevron Technology’ - A Review,” *International Journal of Aeroacoustics*, Vol. 10, Issue 5-6, 2011.
- [²] Xi, H., Tucker, P. and Eastwood, S., “Large Eddy Simulations of Chevron Jet Flows with Noise Predictions,” *International Journal of Heat and Fluid Flow*, Vol. 30, No. 6, 2009.
- [³] Paliath, U., Shen, H., Avancha, R. and Shieh, C., “Large Eddy Simulation for Jets from Chevron and Dual Flow Nozzles. AIAA 2011-2881, 2011.
- [⁴] Uzun, A., Bin, J. and Hussaini, M.Y., “High-Fidelity Numerical Simulation of a Chevron Nozzle Jet Flow,” *International Journal of Aeroacoustics*, Vol. 10, Nos. 5-6, 2011.
- [⁵] Dhamankar, N.S., Blaisdell, G. A., and Lyrintzis, A. S., “Analysis of Turbulent Flow and Associated Noise with Round and Chevron Nozzles using Large Eddy Simulation,” AIAA-2016-3045, 2016.
- [⁶] Stich, G. D., Housman, J. A., Ghate, A. S. and Kiris, C.C., “Jet Noise Prediction for Chevron Nozzle Flows with Wall-Modeled Large-Eddy Simulation,” AIAA-2021-1185, 2021.
- [⁷] Nickerson, M., Ferris, R. and van der Velden, W. C. P., “Simulations of Chevrons on Single Flow How Jets,” AIAA-2019-1837.
- [⁸] Depuru Mohan, N. K., Dowling, A. P., Karabasov, S. A., Xia, H., Graham, O., Hynes, T. P. and Tucker, P. G., “Acoustic Sources and Far-Field Noise of Chevron and Round Jets,” *AIAA Journal*, Vol. 53, No. 9, 2015.
- [⁹] Englom, W. A., Khavaran, A. and Bridges, J., “Numerical Prediction of Chevron Nozzle Noise Reduction using WIND-MGBK Methodology,” AIAA-2004-2079, 2004.
- [¹⁰] Koch, L.D., Bridges, J. and Khavaran, A., “Mean Flow and Noise Predictions for a Separate Flow Jet with Chevron Mixers,” AIAA-2004-0189.
- [¹¹] Birch, S. F., Lyubimov, D. A., Maslov, V. P, and Secundov, A. N., “Noise Prediction for Chevron Nozzle Flows,” AIAA-2006-2600, 2006.
- [¹²] Bridges, J.E. and Podboy, G. G., “Azimuthal Noise Directivity of Non-Axisymmetric Jets,” AIAA 2021-1183, 2021.
- [¹³] Brown, C.A. and Bridges, J.E., “Small Hot Jet Acoustic Rig Validation. In NASA/TM AIAA 2006-214234, 2006.

- [¹⁴] Bridges, J.E and Brown, C.A., “Parametric Testing of Chevrons on Single Flow Hot Jets,” AIAA-2004-2824, 2004.
- [¹⁵] Goldstein, M.E. and Leib, S. J., “The Aeroacoustics of Slowing Diverging Supersonic Jets,” *Journal of Fluid Mechanics*, Vol. 600, pp. 291-337, 2008.
- [¹⁶] Leib, S. J. and Goldstein, M. E., “Hybrid Source Model for Predicting High-Speed Jet Noise,” *AIAA Journal*, Vol. 49, No. 7, 2011.
- [¹⁷] Orszag, S. A. and Bender, C. M., *Advanced Mathematical Methods for Scientists and Engineers*, McGraw-Hill Book Company, New York, 1978, p. 484.
- [¹⁸] Leib, S. J., “Noise Predictions for Rectangular Jets Using a Conformal Mapping Method,” *AIAA Journal*, Vol. 51, No. 3, 2013.
- [¹⁹] Ferziger, J. H. and Perić, M., *Computational Methods for Fluid Dynamics*, 3rd edition, Springer-Verlag Berlin Heidelberg, 2002, pp. 230-239.
- [²⁰] Giuliani, J. E. and Chen, JP, “Fan Response to Boundary-Layer Ingesting Inlet Distortions,” *AIAA Journal*, Vol. 54, No. 10, 2016.
- [²¹] Leib, S. J., “Toward a Finite Volume/Unstructured Grid Approach to Jet Noise Prediction Using the Generalized Acoustic Analogy,” NASA Acoustics Technical Working Group Meeting, October, 2017, Cleveland, Ohio.
- [²²] Papamoschou, D., “Modeling of Noise Reduction in Complex Multistream Jets,” *Journal of Fluid Mechanics*, Vol. 834, 2018, pp. 555-599.
- [²³] Goldstein, M.E., Sescu, A. and Afsar, M.Z., “Effect of non-parallel mean flow on the Green’s function for predicting the low-frequency sound from turbulent air jets,” *Journal of Fluid Mechanics*, Vol. 695, pp. 199-234, 2012.